THE ASTROPHYSICAL JOURNAL, 456:234–249, 1996 January 1

SITES OF RELATIVISTIC PARTICLE ACCELERATION IN SUPERNOVA REMNANT CASSIOPEIA A

M. C. ANDERSON AND L. RUDNICK
Astronomy Department, University of Minnesota, Minneapolis, MN 55455
Received 1995 January 30; accepted 1995 July 11

ABSTRACT

We have determined the synchrotron spectral indices of 304 compact radio knots in the supernova remnant Cassiopeia A. A comparison of these data with the dynamical and brightness properties of these knots tabulated by Anderson & Rudnick indicates that spectral index shows a significant correlation with projected radius from the center of the remnant. Spectrally flat knots reside in a shell coincident with the bright radio ring, while steeper knots occupy a shell coincident with the diffuse radio plateau surrounding the ring. To a lesser extent, we find spectral index to be correlated also with the radio brightness of the knot, in the sense that brighter knots tend to have steeper spectra. No significant correlation is found between spectral index and knot deceleration or rate of brightness change.

As the synchrotron spectral index traces the distribution of energy among relativistic particle populations, we use these results to study the nature of particle acceleration mechanisms active in Cas A. Given the dual-shell nature of the spectral index distribution in Cas A and the lack of strong correlation between spectral index and dynamical properties of the knots, we conclude that radio-bright compact features are *not* sites of currently active particle acceleration in Cas A. This conclusion is in agreement with models of supersonic gaseous bullets constructed by Jones, Kang, & Tregillis. In these models, the marked synchrotron brightening which accompanies bullet deceleration is due primarily to preexisting relativistic particles radiating in rapidly amplifying shear-layer magnetic fields, rather than a large infusion of new relativistic particles accelerated in situ. Spectral variations between compact features in Cas A are more likely to reflect modulations in the background particle energy spectra within the remnant, perhaps instilled by temperature variations in the underlying thermal material. This interpretation requires that the diffuse synchrotron emission show the same spectral variations as seen in compact features; preliminary indications suggest that this is the case.

Subject headings: acceleration of particles — cosmic rays — ISM: individual (Cassiopeia A) — radiation mechanisms: nonthermal — radio continuum: ISM — supernova remnants

1. INTRODUCTION

Studies of the energetics and chemical composition of the Galactic cosmic-ray (CR) population point to Galactic supernova remnants (SNRs) as the most plausible sites for the acceleration of CRs with energies up to 10^{14} eV nucleon^{-1}. Such in situ acceleration in a diffuse plasma is important for extragalactic radio sources as well (e.g., Meisenheimer et al. 1989), and SNRs offer us the opportunity to study such processes in detail. However, the mechanisms for energy exchange between the expanding SNR ejecta and relativistic particles are not well understood. Although various assumptions may be found in the literature (e.g., Bell 1978; Dickel & Greisen 1979; Cowsik & Sarkar 1984), we do not even know where in the complicated remnant structure the bulk of the acceleration takes place, nor what constitutes the seed population for the acceleration mechanism nor how these particles become injected into the acceleration cycle. We do not know how the method and efficiency of acceleration changes as the remnant evolves. It is the purpose of this paper to try to identify sites of active particle acceleration in the young SNR Cassiopeia A and to learn something about the relevant seed population for acceleration.

Our primary tool for studying acceleration processes in Cas A is the spatial variation in the synchrotron spectral index α (where $S_\nu \propto \nu^{-\alpha}$), which is related to the energy distribution among the radiating cosmic-ray electrons. Since the synchrotron lifetimes of electrons in even the brightest radio features in Cas A are on the order of several thousands of years, much older than the remnant, any spectral variations present in the remnant must be due either to non-heating–type energization (relativistic acceleration) processes, or to an intrinsic break in the underlying seed particle energy spectrum.

Unfortunately (for our purposes), multifrequency studies of shell-type supernova remnants have typically found little evidence for spatially varying synchrotron spectra (Scheuer 1984). In those few remnants that do appear to exhibit spectral variations (see Anderson & Rudnick 1993 for a compendium), the range in variation is quite small ($\Delta\alpha \sim 0.2$). The integrated spectrum in Cas A is straight to within ± 0.007 between 81 MHz and 9.4 GHz (Baars et al. 1977), further constraining the distribution of any spectral variations within the remnant. This fact underscores the need for a careful examination of instrumental factors that may contaminate spectral spurious detections of variations.

Several studies of the distribution of the synchrotron spectral index in Cas A are recorded in the literature (see, e.g., Anderson et al. 1991, and references therein). In order to relate spectral variations to specific physical processes, we present spectral index measurements for a sample of 304 radio knots whose dynamical properties were analyzed by Anderson & Rudnick (1995, hereafter AR). We use the radiative and dynamical comparisons to address the following questions: (1) Is relativistic particle acceleration needed to explain the high synchrotron emissivities observed in Cas A? If so, (2) when and where does particle acceleration occur, and through which

mechanisms? Finally, (3) what is the relevant pool from which particles are injected into the acceleration mechanism? What constraints do we have to help define this pool?

In particular, we wish to determine whether bright compact radio features in Cas A are or are not sites of active particle acceleration. This is often assumed to be the case (see, e.g., Cowsik & Sarkar 1984), presumably based in analogy with findings in extragalactic radio jets, where the radio bright regions at the ends of the jets (the "hot spots") are interpreted as sites of active particle acceleration because of their flatter spectra (e.g., Meisenheimer et al. 1989). In Cas A, the steeper spectrum bright compact features could be sites of fresh particle injection. However, our comparison of the evolution of compact features with numerical simulations of shocked clumps (Jones, Kang, & Tregillis 1994) highlighted the importance of the magnetic field growth, as opposed to currently active particle acceleration (Anderson et al. 1994, hereafter AJRTK) in raising the emissivity.

2. SPECTRAL VARIATIONS AMONG SELECTED RADIO KNOTS

As interferometric images are inherently subject to many types of uncertainties not present in single-dish observations, we have gone to great lengths to ascertain the credibility of spectral variations apparent in Cas A. Knot spectral indices computed from independent observations of the source in epochs 1985, 1987, and 1990 have been compared to evaluate the robustness of these measurements and to search for possible secular variations in α.

2.1. *Observations and Image Reconstruction*

The results presented here are derived from radio observations of Cas A conducted with the Very Large Array (VLA[1]; Napier, Thompson, & Ekers 1983) in the nominal L (1.4 GHz) and C (5.0 GHz) frequency bands in 1985, 1987, and 1990. The details of these VLA observing sessions have been summarized by AR (see their Tables 1 and 2).

Owing to the spatial complexity of the remnant, data at each observing band have been obtained in all four standard VLA configurations at each epoch and combined in the final image synthesis (the A-configuration data at C band have been excluded in most cases to match the resolution of the L-band data). To further improve aperture coverage, a technique known as "bandwidth synthesis" was used, whereby data are collected at several frequencies in a narrow band around the nominal frequency. The uncertainties introduced into our measurements of spectral index by the use of bandwidth synthesis are discussed below.

Unfortunately, the epoch 1990 A- and B-configuration observations at L band were contaminated by radio frequency interference, severely degrading their quality (Anderson 1993). Spectral indices computed for epoch 1990 will therefore be used only in a very guarded sense, as a test of the robustness of temporal spectral variations measured between epochs 1985 and 1987.

Calibration and image reconstruction procedures used for all epochs closely follow those applied to the epoch 1987 data, as outlined by Anderson et al. (1991). Dirty maps at each band were deconvolved with the AIPS Maximum Entropy routine VTESS. All images have been corrected for primary beam attenuation and have been convolved with a circular Gaussian function of diameter 1.″3 to fix the resolution.

As an alternative reconstruction method, we have taken advantage of the default image capabilities in VTESS. In this algorithm, the default image defines the brightness distribution of the output image in the absence of any other information. The reconstructed image is therefore constrained to match the default image as closely as possible, while simultaneously requiring the Fourier transform of the reconstructed image to match the observed visibility data, within their uncertainties. By using a scaled (with $\alpha = 0.77$; Baars et al. 1977) and primary-beam corrected version of the L-band map as the default image for the C-band map reconstruction at each epoch, we then obtain spectral variations only where they are forced by the data.

2.2. *Uncertainties in Bandwidth-synthesized Images*

While bandwidth synthesis may be an attractive means to increasing aperture coverage for complex sources, it introduces sources of uncertainty not present in single-frequency observations. First, each frequency requires a slightly different primary beam attenuation correction. Second, each frequency in the synthesized bandwidth will produce a slightly different visibility amplitude for a given u-v cell if the source has a nonzero spectral index. Here we estimate the errors in reconstructed flux density introduced by these effects.

A nominal frequency can be assigned to each epoch's observations by averaging over all frequencies contained in the synthesized band. Because total integration time varies between array configurations in these observations, we have weighted the average by the number of visibilities collected at each frequency. The rms in the distribution of frequencies for a given epoch has been similarly weighted. The following nominal frequencies are thus computed for epochs 1985 and 1987:

$$\nu_{85_C} = 4804 \pm 29 \text{ MHz},$$
$$\nu_{85_L} = 1494 \pm 10 \text{ MHz},$$
$$\nu_{87_C} = 4809 \pm 28 \text{ MHz},$$
$$\nu_{87_L} = 1517 \pm 10 \text{ MHz}.$$

Given the range in frequencies used in these observations, the primary beam effect is negligible in comparison with residual sidelobe and receiver noise contributions. At the radius of the bright radio ring ($\sim 100''$), the ratio of primary beam correction factors for frequencies ν and $\nu + d\nu$ is unity within $\sim 0.1\%$ at C band and 0.01% at L band.

The finite bandwidth also introduces a spread in the measured total intensities, which we can approximate as follows:

$$\frac{\sigma_S}{S} = \frac{\alpha\,\delta\nu}{\nu}, \tag{1}$$

where $S(\nu) = S_0\,\nu^{-\alpha}$ over the rms bandwidth $\delta\nu$. The value of σ_S/S is on the order 0.5% for both the L and C bands, assuming an average spectral index of $\alpha = 0.77$. This term can be incorporated into the standard error equation to give a full expression for the dominant uncertainties in α:

$$(\delta\alpha)^2 = \frac{1}{[\ln(\nu_L/\nu_c)]^2}\left[\frac{\sigma_L^2}{S_L^2} + \frac{\sigma_C^2}{S_C^2} + \alpha^2\left(\frac{\delta\nu_1^2}{\nu_1^2} + \frac{\delta\nu_2^2}{\nu_2^2}\right)\right], \tag{2}$$

where σ_X represents the noise contributed at band X by the

[1] The Very Large Array is a facility of the National Radio Astronomy Observatory, operated by Associated Universities, Inc., under contract with the National Science Foundation.

receiver system and residual sidelobes in the input images. The bandwidth term proved to be inconsequential and is therefore neglected in the errors quoted below.

2.3. *Image Normalization*

The normalization procedure described below has been applied to all images under investigation here to force spectral maps at all epochs to a common mean index. This method of normalization was devised to compensate for differences in absolute flux calibration between epochs, and for differences in image reconstruction resulting from inconsistencies in u-v coverage.

Radial intensity profiles, created by averaging pixel brightness in annular bins of width 5″ around the center of the main radio ring, were computed for all six images. The radial intensity profile taken from the 1987 L-band image (the image of highest quality) served as the standard for normalization; the 1985 and 1990 L-band profiles were fitted to this fiducial profile to obtain a scale factor (S), a radial term (A), and a constant offset, $L_{85,90} = S_{85,90} L_{87} + A_{85,90} \times \text{radius} + \text{constant}_{85,90}$. The C-band profiles were similarly fitted to the fiducial profile, assuming a scaling factor given by the integrated spectral index of the remnant (0.77; Baars et al. 1977). This process was repeated for the C-band images reconstructed with L-band defaults.

The purpose of these corrections is to force all images, at all epochs and frequencies, to be as similar to each other as possible on large scales. This normalization should minimize any instrumentally induced spectral changes that occur on scales larger than $\sim 5''$. We also would not be able to detect any real steepening in the diffuse emission beyond the bright ring, as was suggested by Kassim et al. (1995). In fact, since we would correct for this effect, any steepening we see in the small-scale features beyond the ring would then be even stronger than we quote.

In normalizing, we also lose all information concerning the integrated spectral index at any given epoch. Note that the secular flattening in the integrated spectral index of Cas A reported by Baars et al. (1977),[2] at a rate of 0.0013 per year, would be negligible over the time frame studied here (5 years).

2.4. *Measurement of Spectral Indices for Knot Sample*

Spectral indices computed through a straightforward division of two interferometric images should be considered suspect, given the uncertainties inherent in the image reconstruction process. Differences in u-v coverage between bands can potentially generate artificial large-scale background fluctuations between the images, mimicking spectral variations. To eliminate this problem, we have used a least-squares determination of scaling factors between pixel intensities at L and C bands within regions surrounding each knot in the sample; all spectral indices quoted in this work, unless otherwise specified, have been computed from these scaling factors.

The least-squares method employed here is similar to that used by Tuffs (1986) and AR to measure the proper motions of compact radio features in Cas A. In the current application, we minimize the quantity

$$T(\xi) = \sum_{i=1}^{I} \sum_{j=1}^{J} Q_{ij}^2(\xi) , \qquad (3)$$

where

$$Q_{ij}(\xi) = L_{ij} - SC_{ij} - H , \qquad (4)$$

in summation over the specified region (of size $I \times J$ pixels). Here $L_{i,j}$ and $C_{i,j}$ represent the intensities in the i–jth pixel at L and C bands, respectively. For each knot, equation (3) was minimized with respect to the vector $\xi = (S, H)$, where S is the intensity scaling factor for the knot between the L- and C-band images. The parameter H absorbs any offsets between the two images on scales larger than that of the specified regression region which may result from incomplete reconstruction. The GX and GY terms included by Tuffs (1986) and AR have been eliminated here to reduce the number of degrees of freedom allowed for the fit. The spectral index, α, is computed from the best-fit value of S [$\alpha = \ln(S)/\ln(\nu_L/\nu_C)$].

Errors in α were determined by varying S and H according to the method described by Avni (1976), assuming 2 degrees of freedom. Spectral indices were computed with and without intensity normalization to verify that the normalization procedure itself was not introducing sporadic variations.

2.5. *Results*

The knot spectral indices derived for epoch 1987 are tabulated in Table 1. These spectra have been computed using C-band Maximum Entropy images reconstructed with L-band default images; all images have been normalized according to the procedure described in § 2.3.

Figure 1 displays the spatial distribution of the epoch 1987 knot spectral indices. This distribution is qualitatively similar to the spectral map presented by Anderson et al. (1991), computed from a ratio of images at L and C bands. The regression method, however, yields a wider distribution of spectral indices, since the diluting effect of the large-scale background is removed. The average knot spectral index is 0.77 for epoch 1987, as defined by the normalization process; typical uncertainties in α for each knot are of order ± 0.03.

The color plate in Figure 2 (Plate 11) gives a more visual representation of the spatial distribution of spectral indices among compact features in Cas A. Here, instead of placing a separate regression box around each knot, a regression window of size 16.″4 × 16.″4 was slid across the entire remnant,

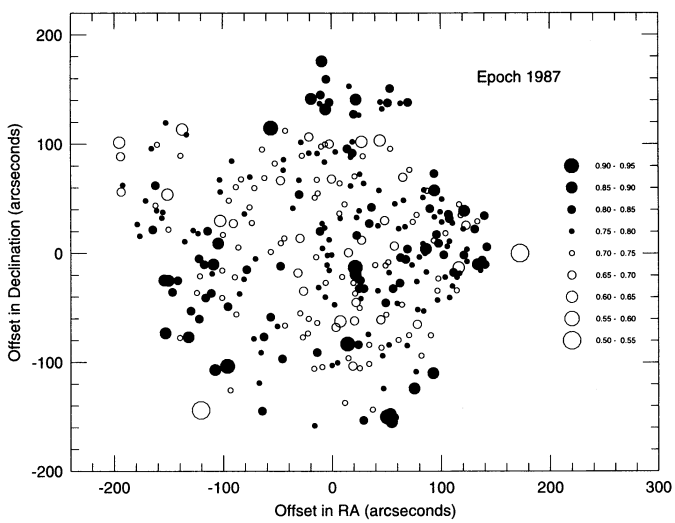

FIG. 1.—Spatial distribution of knot spectral indices, epoch 1987

[2] See, however, the contradictory findings of Hook, Duffet-Smith, & Shakeshaft (1992), who find no evidence for secular flattening.

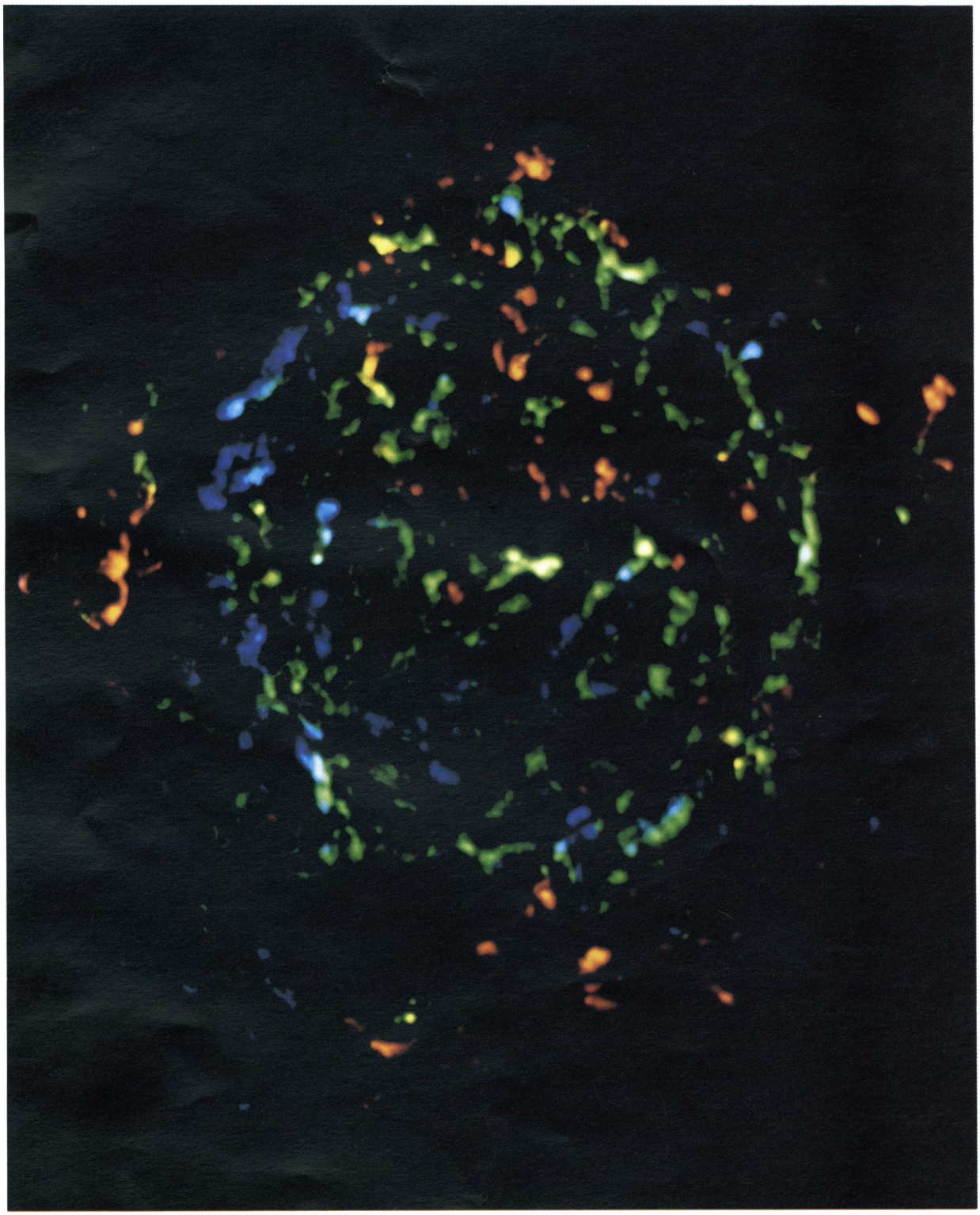

FIG. 2.—Spatial distribution of α_{rcg} distribution: epoch 1985. The range in spectral index displayed here runs from 0.75 (blue) to 0.9 (red).

ANDERSON & RUDNICK (see 456, 236)

TABLE 1

RADIO KNOT SPECTRAL INDICES (EPOCH 1987)

Knot	Knot$_T$	x	y	Box$_{x1}$	Box$_{y1}$	Box$_{x2}$	Box$_{y2}$	α	$\delta alpha$
1	9	-106.8	-135.7	-119.0	-141.8	-103.4	-129.8	0.52	0.06
2	15	-79.8	-117.2	-86.2	-122.2	-75.0	-109.4	0.70	0.02
3	20	-53.4	-110.6	-57.8	-116.6	-49.8	-108.2	0.76	0.04
4	6	-50.5	-136.4	-58.2	-142.2	-45.0	-131.4	0.85	0.03
5	1	-2.6	-149.9	-9.8	-156.6	4.6	-147.0	0.76	0.04
6	12	25.5	-128.9	20.6	-132.6	31.0	-123.4	0.73	0.02
7	3	42.7	-144.8	37.4	-153.0	45.0	-142.6	0.83	0.01
8	7	51.1	-135.1	44.6	-139.4	55.0	-129.8	0.74	0.02
9	14	61.0	-115.8	54.6	-123.4	67.8	-111.0	0.79	0.01
10	4	64.6	-141.8	60.2	-145.4	67.4	-139.4	0.91	0.01
11		67.4	-139.0	64.6	-141.8	71.4	-134.2	0.90	0.01
12		68.6	-146.6	64.6	-149.8	72.2	-144.2	0.86	0.01
13		71.0	-142.2	67.8	-145.0	74.6	-139.4	0.84	0.01
14	17	89.3	-115.5	84.6	-122.2	95.8	-108.6	0.86	0.02
15	61	-139.2	-64.9	-143.4	-69.4	-136.2	-61.0	0.86	0.02
16	59	-125.9	-69.2	-129.4	-73.0	-122.2	-65.8	0.70	0.05
17	49	-118.0	-68.6	-121.4	-73.0	-114.6	-65.8	0.87	0.05
18	78	-115.8	-44.6	-118.2	-49.4	-111.8	-39.8	0.81	0.03
19	75	-108.2	-51.8	-112.6	-56.6	-103.8	-47.4	0.81	0.06
20	97	-102.2	-32.5	-106.2	-36.2	-99.0	-29.4	0.83	0.03
21	101	-97.0	-28.2	-101.0	-33.0	-93.4	-23.8	0.84	0.03
22		-93.6	-98.6	-98.2	-104.2	-89.0	-95.0	0.87	0.02
23		-87.1	-32.4	-92.2	-36.6	-83.4	-28.2	0.75	0.01
24	31	-82.4	-95.2	-86.2	-99.8	-79.4	-92.2	0.91	0.05
25	83	-81.9	-40.5	-86.2	-44.6	-78.2	-37.0	0.83	0.02
26		-74.3	-47.6	-78.2	-51.0	-71.0	-44.6	0.71	0.02
27	99	-71.4	-28.7	-76.6	-32.6	-67.4	-25.0	0.79	0.02
28		-58.3	-70.0	-62.2	-74.2	-53.8	-65.8	0.77	0.02
29	41	-51.8	-82.6	-55.4	-86.6	-48.6	-78.6	0.78	0.01
30	51	-48.9	-68.3	-55.0	-72.6	-44.2	-63.0	0.82	0.02
31	72	-43.0	-50.2	-46.2	-52.6	-39.0	-46.2	0.83	0.06
32	60	-36.6	-58.6	-40.2	-61.8	-32.6	-55.0	0.77	0.03
33	34	-32.2	-88.2	-37.4	-91.8	-27.8	-83.0	0.83	0.02
34	63	-29.8	-57.8	-33.4	-61.0	-25.4	-53.8	0.72	0.03
35		-15.9	-46.6	-20.2	-50.2	-12.2	-43.4	0.73	0.03
36	53	-13.4	-68.6	-17.4	-75.4	-9.8	-64.2	0.74	0.02
37	57	-8.8	-65.1	-12.2	-69.0	-1.8	-60.6	0.73	0.02
38		-8.0	-51.6	-11.4	-55.0	-5.4	-48.2	0.70	0.03
39	32	-3.0	-97.4	-7.0	-101.8	1.0	-93.4	0.71	0.02
40	39	-0.2	-82.6	-4.2	-87.4	4.2	-78.2	0.81	0.03
41	64	-0.2	-55.4	-3.4	-59.0	4.6	-51.8	0.73	0.02
42	27	4.5	-95.8	-0.2	-102.2	7.8	-93.8	0.71	0.02
43	92	7.2	-31.5	5.0	-34.2	10.2	-28.2	0.77	0.02
44	29	13.5	-94.3	8.2	-98.2	18.6	-90.2	0.78	0.01
45	87	15.8	-38.6	12.6	-42.2	19.4	-33.8	0.79	0.01
46		17.2	-59.5	13.8	-62.6	20.2	-56.6	0.69	0.03
47	30	18.6	-92.0	16.2	-93.4	23.0	-87.0	0.76	0.01
48		21.2	-53.9	19.0	-56.6	23.4	-51.0	0.63	0.13
49	48	27.9	-74.7	22.2	-80.2	33.0	-70.6	0.91	0.01
50	40	28.6	-87.8	24.6	-89.8	33.8	-82.6	0.75	0.05
51	28	32.7	-95.0	28.6	-100.6	36.6	-91.8	0.70	0.02
52		34.2	-53.6	30.6	-56.2	38.2	-50.6	0.68	0.08
53	98	34.8	-28.3	32.2	-30.6	37.8	-25.8	0.73	0.03
54		35.6	-36.5	33.4	-39.8	37.8	-33.4	0.65	0.06
55	47	37.8	-75.4	33.8	-79.4	40.6	-73.0	0.84	0.03
56	84	39.0	-41.6	36.6	-44.6	41.4	-39.0	0.73	0.04
57	25	39.1	-97.0	35.0	-104.6	44.2	-94.2	0.75	0.01
58	95	40.2	-33.0	36.6	-36.2	43.4	-30.2	0.77	0.03
59	52	46.9	-66.0	43.0	-70.2	51.0	-61.4	0.76	0.02
60	33	47.6	-93.0	43.4	-99.4	53.4	-87.8	0.75	0.01
61	42	47.8	-75.4	45.0	-78.2	52.6	-71.8	0.73	0.02

TABLE 1—*Continued*

Knot	$Knot_T$	x	y	Box_{x1}	Box_{y1}	Box_{x2}	Box_{y2}	α	$\delta alpha$
62	66	58.4	-52.5	54.6	-56.6	61.8	-49.4	0.69	0.04
63	45	59.0	-78.2	54.6	-82.2	63.0	-73.0	0.72	0.02
64	37	60.1	-85.5	56.6	-89.0	63.8	-83.0	0.80	0.06
65	89	63.0	-37.0	58.6	-41.4	67.4	-33.0	0.81	0.03
66	74	63.4	-47.8	59.0	-51.8	67.4	-43.8	0.70	0.03
67		65.8	-75.4	62.2	-79.0	70.6	-71.0	0.79	0.04
68		73.4	-37.4	70.2	-39.8	75.8	-34.2	0.76	0.04
69		74.6	-71.0	71.8	-74.2	76.6	-68.2	0.73	0.02
70	86	77.8	-38.6	75.0	-43.4	81.0	-34.2	0.74	0.02
71	43	82.6	-76.2	77.4	-83.0	89.0	-69.8	0.75	0.01
72	55	84.2	-66.6	79.4	-70.6	88.2	-62.6	0.73	0.02
73	26	90.8	-100.2	87.0	-104.2	96.2	-91.8	0.80	0.03
74	62	91.8	-56.6	88.6	-61.4	95.4	-52.2	0.68	0.03
75	81	92.2	-43.0	87.0	-45.4	95.8	-37.4	0.78	0.01
76	36	95.5	-85.5	88.6	-92.6	101.4	-81.0	0.75	0.02
77	80	97.5	-44.4	95.0	-47.4	101.0	-41.4	0.75	0.04
78	54	104.1	-66.7	100.2	-74.2	108.6	-62.6	0.74	0.01
79	23	106.6	-101.4	100.2	-108.6	113.8	-93.0	0.85	0.02
80	96	110.2	-34.2	106.6	-39.8	113.8	-29.4	0.77	0.01
81		121.2	-31.9	117.8	-36.2	125.4	-29.0	0.79	0.01
82	209	-165.0	35.0	-167.8	29.4	-161.8	40.6	0.76	0.02
83	194	-162.6	24.2	-166.2	18.2	-159.0	27.8	0.76	0.02
84	200	-150.6	29.8	-155.8	25.0	-147.0	34.2	0.83	0.04
85		-148.1	52.2	-150.6	49.8	-145.4	55.8	0.74	0.03
86	230	-147.1	47.5	-150.6	43.8	-143.8	50.6	0.77	0.01
87	220	-142.2	40.7	-145.8	37.4	-138.6	44.2	0.80	0.02
88		-141.4	46.2	-144.2	43.4	-138.6	49.4	0.79	0.02
89	118	-140.2	-16.3	-143.4	-19.4	-138.2	-12.6	0.87	0.02
90	120	-136.2	-16.6	-138.2	-24.6	-132.2	-11.0	0.85	0.02
91	206	-136.2	30.2	-139.4	26.6	-132.6	33.8	0.71	0.08
92	104	-132.5	-27.3	-135.8	-31.0	-129.0	-24.2	0.82	0.02
93	123	-127.8	-16.6	-131.0	-19.8	-124.6	-12.6	0.85	0.02
94	186	-121.4	19.2	-128.6	11.8	-117.4	25.8	0.80	0.01
95	201	-113.4	29.4	-116.6	25.8	-111.4	33.4	0.79	0.10
96		-110.2	-27.8	-113.8	-31.4	-107.8	-23.4	0.75	0.04
97		-109.0	26.6	-111.8	23.4	-106.6	29.0	0.76	0.13
98	157	-108.2	3.4	-112.2	1.0	-104.6	6.6	0.81	0.03
99	126	-107.4	-12.6	-112.6	-17.8	-105.0	-10.2	0.74	0.04
100	150	-103.4	-2.0	-107.0	-6.2	-99.0	2.2	0.82	0.01
101		-100.2	28.6	-105.4	24.6	-96.2	32.6	0.80	0.04
102	130	-96.2	-10.2	-101.8	-17.0	-92.6	-7.4	0.77	0.01
103	152	-94.9	-1.7	-97.4	-3.8	-91.8	1.8	0.88	0.03
104	181	-90.7	17.4	-93.8	13.4	-87.4	21.0	0.85	0.04
105	217	-88.6	38.2	-92.2	34.2	-85.0	42.2	0.65	0.03
106	136	-86.9	-7.3	-92.6	-12.2	-82.6	-3.4	0.75	0.02
107	198	-86.2	25.4	-90.2	21.0	-82.6	31.0	0.73	0.02
108	211	-76.6	35.8	-81.0	27.8	-72.6	39.8	0.69	0.03
109	124	-75.4	-13.4	-79.4	-18.2	-73.0	-9.0	0.75	0.02
110	179	-72.2	13.8	-78.2	9.8	-68.6	18.2	0.72	0.04
111	121	-67.0	-15.4	-70.6	-19.0	-62.2	-10.2	0.79	0.02
112	228	-66.6	44.6	-69.4	41.0	-61.0	49.0	0.77	0.03
113	141	-64.5	-6.4	-67.0	-9.4	-61.0	-3.0	0.81	0.06
114		-61.8	50.6	-65.0	47.0	-58.6	53.8	0.73	0.03
115	214	-59.8	36.2	-65.0	30.2	-56.2	39.4	0.74	0.04
116	156	-56.6	3.4	-59.4	0.2	-51.8	7.4	0.79	0.02
117	170	-42.6	9.8	-49.0	5.0	-40.2	13.8	0.73	0.05
118	148	-33.8	-3.2	-37.8	-7.4	-30.6	0.2	0.81	0.06
119		-33.4	17.8	-37.4	14.6	-31.0	21.0	0.72	0.04
120	192	-30.2	22.2	-33.0	18.6	-26.2	26.6	0.74	0.05
121	234	-22.2	49.8	-27.0	45.0	-17.0	53.8	0.75	0.03
122	138	-17.8	-9.5	-22.2	-13.4	-14.2	-6.2	0.67	0.05

TABLE 1—*Continued*

Knot	Knot_T	x	y	Box_{x1}	Box_{y1}	Box_{x2}	Box_{y2}	α	$\delta alpha$
123	191	-15.8	22.2	-19.0	15.8	-9.8	25.4	0.65	0.04
124	105	-12.7	-26.2	-17.0	-31.4	-9.8	-23.4	0.67	0.07
125	162	-1.0	5.0	-4.2	1.4	2.2	7.8	0.70	0.05
126	112	1.3	-22.7	-2.2	-27.0	5.8	-17.8	0.77	0.02
127		2.6	28.6	-0.6	25.4	6.2	32.6	0.80	0.04
128	210	4.6	35.8	0.6	33.8	9.0	41.8	0.79	0.02
129	173	5.0	13.0	1.0	9.4	9.0	17.0	0.77	0.02
130		7.0	31.8	4.6	28.6	11.0	35.4	0.80	0.03
131	119	7.7	-18.5	4.6	-21.4	11.4	-15.4	0.72	0.04
132	145	9.0	-2.2	5.0	-4.2	11.4	-0.2	0.79	0.01
133	164	9.4	6.6	5.8	3.8	11.4	10.2	0.77	0.02
134	188	11.0	21.0	6.6	17.0	14.6	24.6	0.75	0.03
135		11.0	-7.0	8.6	-11.0	13.0	-5.0	0.76	0.02
136		13.3	7.1	10.6	3.8	17.0	10.6	0.78	0.01
137	232	20.6	45.0	17.0	41.8	24.2	49.4	0.71	0.03
138	223	21.4	40.6	17.8	37.4	24.6	43.8	0.75	0.05
139	132	22.9	-13.2	19.4	-16.2	26.2	-9.0	0.72	0.07
140	169	28.9	9.1	26.2	6.6	32.2	12.6	0.66	0.11
141		33.3	-18.6	30.2	-21.4	36.2	-14.2	0.74	0.03
142		35.1	-4.4	31.8	-7.8	38.2	-1.4	0.94	0.03
143		35.4	-11.0	31.4	-14.6	41.4	-7.4	0.86	0.04
144	193	36.6	25.0	34.2	22.2	40.6	29.0	0.82	0.04
145	224	36.6	41.4	32.2	37.0	39.8	44.6	0.78	0.02
146	111	38.6	-23.8	35.8	-26.2	40.6	-20.6	0.81	0.03
147		39.0	47.4	35.4	44.6	42.2	50.6	0.76	0.04
148		39.8	-16.2	37.0	-19.8	43.4	-12.6	0.84	0.03
149		41.0	20.6	39.0	17.8	45.4	25.8	0.67	0.05
150	109	43.0	-23.8	40.6	-26.6	46.2	-21.0	0.82	0.02
151	212	48.2	35.9	45.0	32.6	50.6	39.0	0.84	0.04
152	235	50.2	50.6	45.4	46.2	53.4	54.6	0.82	0.02
153		53.4	-2.2	49.8	-5.4	57.4	1.8	0.73	0.03
154	102	55.8	-25.8	53.4	-33.0	60.2	-19.8	0.75	0.02
155	204	56.2	33.8	51.0	31.0	60.2	37.0	0.77	0.03
156	215	62.2	38.6	59.4	35.4	65.8	41.8	0.70	0.03
157		62.9	-2.6	60.2	-5.4	65.0	-0.6	0.74	0.04
158	154	65.4	0.4	63.0	-2.2	68.6	3.4	0.72	0.03
159		66.1	-9.1	63.0	-13.8	69.8	-5.8	0.78	0.03
160	110	69.7	-23.8	65.0	-29.8	73.8	-18.6	0.82	0.01
161		71.1	15.2	69.8	13.8	74.2	17.8	0.68	0.09
162	203	75.1	31.1	70.6	27.0	78.6	34.2	0.78	0.02
163	117	76.0	-18.8	72.6	-21.8	79.8	-15.4	0.83	0.01
164	163	76.6	4.6	73.0	1.8	81.8	9.4	0.83	0.01
165	207	80.9	32.8	77.8	29.4	84.2	35.8	0.79	0.05
166	147	81.4	3.0	79.4	-2.2	85.0	5.4	0.80	0.02
167	172	83.0	12.6	77.8	8.2	89.0	15.4	0.81	0.02
168	144	87.0	-2.2	84.6	-7.0	91.4	0.2	0.78	0.02
169	216	87.9	37.2	84.2	33.8	91.4	40.6	0.75	0.03
170	122	91.4	-17.4	86.2	-22.6	97.4	-12.2	0.79	0.02
171	227	91.4	43.8	88.2	40.2	93.8	46.2	0.70	0.04
172	160	93.8	5.0	89.0	0.2	96.6	6.6	0.76	0.03
173	180	97.2	17.4	94.2	14.6	99.8	21.0	0.77	0.04
174		98.9	8.6	96.2	5.8	101.0	11.4	0.80	0.03
175	171	99.8	12.6	97.0	10.6	103.4	16.2	0.86	0.04
176	131	100.0	-8.5	96.6	-10.2	101.8	-5.4	0.75	0.03
177	233	103.4	49.4	99.0	45.4	107.0	52.6	0.81	0.04
178	187	107.0	20.2	103.8	17.4	109.8	23.0	0.72	0.03
179		107.8	41.8	105.0	38.6	111.4	45.4	0.80	0.05
180		109.5	25.8	106.6	22.2	113.8	29.0	0.80	0.03
181		110.2	-25.8	107.4	-29.0	113.8	-23.4	0.73	0.03
182		111.0	-14.6	107.4	-17.4	113.8	-11.0	0.72	0.04
183		111.4	17.6	108.2	13.8	115.0	21.0	0.84	0.05

TABLE 1—*Continued*

Knot	$Knot_T$	x	y	Box_{x1}	Box_{y1}	Box_{x2}	Box_{y2}	α	$\delta alpha$
184		113.0	46.6	109.4	43.4	115.4	50.2	0.76	0.02
185		114.4	37.1	111.0	34.2	118.2	40.2	0.75	0.02
186	161	116.2	7.1	112.2	2.2	121.4	11.0	0.82	0.01
187	127	117.2	-13.2	111.8	-19.4	119.8	-10.6	0.76	0.02
188	199	117.8	27.0	115.0	24.2	121.4	30.6	0.74	0.05
189	177	119.4	14.9	115.8	11.8	122.2	18.2	0.77	0.02
190	231	120.6	44.2	117.0	41.8	123.4	47.0	0.83	0.02
191	218	121.4	40.2	118.2	37.4	124.2	43.4	0.84	0.03
192		121.4	19.6	117.8	17.4	125.0	23.0	0.77	0.03
193		123.9	-21.5	121.0	-23.8	126.6	-18.6	0.79	0.02
194		124.2	36.2	120.2	32.2	127.4	39.8	0.79	0.02
195	135	125.0	-9.0	121.0	-12.2	128.2	-5.4	0.81	0.02
196		127.9	-25.5	124.6	-29.0	131.0	-22.2	0.75	0.02
197	129	128.2	-13.4	124.6	-15.8	130.2	-11.0	0.78	0.02
198	142	129.7	-4.5	126.6	-7.8	132.2	-2.2	0.64	0.05
199		130.6	-9.8	127.8	-13.0	134.2	-7.0	0.78	0.02
200	226	131.8	43.4	128.6	40.6	135.0	46.6	0.70	0.07
201		134.0	30.8	130.2	26.6	136.6	33.0	0.77	0.04
202	168	134.6	6.9	131.0	2.6	138.6	11.4	0.81	0.01
203		135.0	47.4	132.2	45.0	137.8	50.2	0.87	0.03
204		136.6	34.2	134.6	31.8	140.2	37.8	0.69	0.08
205	151	137.4	1.0	134.2	-2.2	139.8	3.4	0.76	0.03
206		137.4	12.2	134.6	9.8	141.0	16.2	0.76	0.01
207	202	144.6	30.6	139.0	24.6	147.8	35.8	0.81	0.01
208		147.0	37.8	143.4	34.2	150.6	41.4	0.74	0.04
209	146	147.3	-1.6	143.4	-6.2	151.4	2.2	0.85	0.02
210	139	149.8	-7.1	147.4	-11.0	152.2	-5.0	0.80	0.02
211	159	151.4	2.2	148.6	1.0	154.6	7.4	0.83	0.02
212	225	153.4	43.0	150.6	39.8	157.8	47.0	0.83	0.05
213	149	154.1	-1.8	150.2	-6.6	157.8	1.4	0.83	0.01
214		155.6	14.3	151.8	10.6	159.0	18.2	0.81	0.03
215		186.2	8.6	181.8	4.6	190.6	12.2	0.54	0.08
216		-181.4	109.8	-184.2	107.0	-177.4	113.0	0.62	0.03
217		-180.2	97.0	-183.8	93.4	-177.0	100.6	0.69	0.12
218		-179.8	64.6	-183.0	61.8	-176.2	67.4	0.68	0.04
219		-178.3	70.8	-181.4	67.8	-174.6	74.2	0.76	0.05
220	242	-157.4	56.6	-163.0	52.2	-155.4	59.4	0.78	0.01
221		-151.8	104.2	-154.2	101.8	-149.8	108.2	0.79	0.08
222	264	-148.2	70.6	-151.0	66.2	-143.4	74.6	0.81	0.03
223		-146.6	107.8	-150.6	103.4	-142.2	112.2	0.74	0.05
224	318	-138.6	127.8	-143.0	122.2	-135.0	131.0	0.79	0.05
225	253	-137.0	62.2	-141.0	58.6	-133.4	65.8	0.61	0.11
226	297	-125.0	97.8	-130.2	94.2	-121.0	104.2	0.72	0.05
227		-123.4	121.8	-127.0	119.0	-119.0	125.4	0.61	0.04
228	315	-119.4	117.0	-125.4	111.8	-115.0	122.2	0.79	0.02
229	273	-89.0	75.8	-94.6	72.2	-84.2	80.2	0.77	0.02
230	257	-88.6	64.6	-91.8	60.6	-84.6	68.6	0.79	0.02
231	244	-80.6	56.6	-83.8	53.4	-77.8	60.2	0.74	0.02
232	289	-77.8	93.0	-82.6	89.8	-74.2	98.6	0.79	0.05
233	267	-74.2	69.0	-77.8	65.8	-68.2	72.6	0.72	0.02
234	275	-69.4	76.2	-77.4	72.6	-65.4	80.6	0.75	0.01
235	278	-61.4	78.2	-66.6	72.6	-52.6	81.0	0.75	0.01
236	263	-57.4	68.2	-61.4	64.2	-55.0	71.0	0.70	0.03
237	300	-50.2	103.4	-54.6	99.0	-46.6	107.8	0.74	0.04
238	279	-48.2	77.4	-51.4	73.8	-43.8	80.2	0.74	0.01
239	317	-42.2	123.0	-46.6	118.6	-38.6	126.6	0.93	0.04
240		-38.6	90.6	-42.6	86.6	-35.8	95.4	0.73	0.02
241		-33.4	75.0	-37.0	71.0	-30.6	77.8	0.68	0.03
242	283	-31.0	84.6	-35.4	81.4	-27.4	88.6	0.77	0.02
243		-30.6	94.2	-35.8	91.0	-25.4	98.2	0.79	0.01
244	316	-29.0	120.6	-33.0	117.8	-24.6	125.8	0.75	0.03

TABLE 1—*Continued*

Knot	Knot_T	x	y	Box_{x1}	Box_{y1}	Box_{x2}	Box_{y2}	α	$\delta alpha$
245	252	-16.6	62.2	-21.0	57.8	-12.2	66.2	0.81	0.03
246	272	-16.6	75.4	-19.8	72.6	-13.4	79.8	0.75	0.04
247	310	-14.6	110.2	-19.8	108.2	-11.0	114.6	0.78	0.03
248		-13.8	97.8	-17.4	94.2	-10.2	101.0	0.74	0.01
249	294	-7.4	100.2	-11.4	97.0	-3.4	103.8	0.75	0.02
250	314	-7.4	115.0	-10.6	113.0	-4.6	119.0	0.68	0.05
251		-2.2	59.4	-5.8	57.4	-0.6	62.6	0.72	0.05
252	276	-0.2	75.8	-3.8	71.8	3.4	79.8	0.71	0.03
253	292	0.2	99.8	-3.8	94.6	3.0	102.6	0.77	0.04
254	254	0.6	63.4	-2.6	61.0	3.4	66.6	0.72	0.04
255		3.8	106.2	0.6	103.0	5.4	110.2	0.70	0.02
256	290	7.0	92.2	1.0	87.0	11.8	99.0	0.75	0.01
257	309	7.4	108.2	5.0	104.2	9.8	111.8	0.72	0.03
258	308	11.4	108.6	9.0	105.4	13.8	111.8	0.69	0.04
259	343	13.4	76.6	9.0	73.0	17.4	80.6	0.70	0.02
260		17.0	101.4	13.0	97.8	21.4	105.4	0.78	0.04
261	277	21.0	72.6	16.6	69.8	24.6	75.8	0.75	0.01
262	237	25.4	53.4	22.2	50.6	28.6	57.4	0.75	0.03
263	302	27.8	104.2	24.2	101.0	31.4	108.2	0.84	0.02
264	271	31.0	70.2	27.0	67.4	33.8	73.4	0.76	0.02
265		31.0	96.6	26.6	93.0	33.4	100.2	0.77	0.02
266	293	32.6	100.2	31.0	98.6	35.8	103.8	0.82	0.05
267	313	32.6	110.6	30.2	108.2	37.4	119.4	0.75	0.01
268	281	34.6	79.0	31.8	77.0	37.4	83.0	0.72	0.06
269		39.4	81.0	36.6	77.8	42.6	84.2	0.76	0.07
270		41.0	110.6	37.0	106.6	44.2	113.0	0.64	0.07
271	298	42.2	97.4	38.2	93.0	47.0	101.8	0.74	0.01
272	265	43.0	72.6	39.0	69.0	47.4	75.0	0.79	0.07
273	256	57.0	66.2	53.0	62.6	60.2	69.8	0.80	0.03
274	311	57.8	111.8	54.2	109.4	60.6	115.4	0.64	0.09
275	305	67.4	104.2	63.4	100.6	71.8	107.8	0.75	0.01
276	243	71.8	53.8	67.8	50.2	75.4	56.6	0.78	0.01
277	280	79.0	78.2	75.8	74.2	81.8	80.6	0.67	0.03
278	247	79.4	57.0	75.4	53.0	83.4	61.4	0.80	0.01
279		85.0	85.0	80.2	81.8	87.8	89.4	0.75	0.02
280	251	97.4	59.8	93.4	56.6	101.0	63.0	0.77	0.01
281		98.2	66.6	94.6	64.2	99.4	69.4	0.75	0.02
282		101.0	65.8	99.0	64.2	102.6	69.0	0.74	0.02
283	259	104.6	65.4	102.2	62.2	105.8	68.6	0.79	0.03
284	282	107.4	81.4	104.6	79.4	111.0	85.4	0.81	0.02
285		107.8	66.2	106.2	63.4	110.6	69.0	0.85	0.04
286	250	114.6	58.2	111.0	54.6	118.6	62.6	0.75	0.03
287		130.4	53.3	127.8	49.8	133.0	56.6	0.74	0.03
288	335	-5.4	149.8	-10.6	145.8	-1.8	155.0	0.85	0.02
289	329	2.6	145.4	-2.2	143.4	6.6	149.4	0.80	0.01
290		3.4	153.4	1.0	150.6	5.8	156.6	0.83	0.02
291	342	4.6	184.2	0.6	180.2	9.4	186.6	0.88	0.02
292	323	7.8	140.2	5.8	129.4	19.4	142.2	0.86	0.01
293		8.6	167.8	4.2	163.8	11.8	171.0	0.80	0.07
294	332	11.4	146.6	7.8	142.6	16.2	150.6	0.82	0.01
295	339	29.8	161.4	26.6	158.2	33.4	164.6	0.76	0.02
296	322	33.8	135.8	30.2	131.4	36.2	138.2	0.81	0.01
297	334	35.8	149.4	32.2	146.2	40.6	153.8	0.89	0.03
298	321	38.6	135.0	35.4	131.4	41.8	138.2	0.77	0.02
299	330	58.2	147.0	56.2	145.0	61.4	150.2	0.75	0.02
300	324	59.8	140.6	55.8	137.4	63.8	144.6	0.77	0.02
301		65.0	146.2	63.0	143.8	67.8	149.4	0.82	0.03
302	337	67.0	159.4	63.8	155.4	70.6	163.4	0.84	0.05
303	327	76.6	145.8	73.4	141.8	80.6	148.6	0.77	0.08
304	328	83.4	146.6	79.8	143.4	86.2	150.6	0.83	0.04

using the 1985 data. An intensity scaling factor S was then determined at each box position, and the corresponding value of α was assigned to the center pixel. The window size used here was chosen to filter out the apparent large-scale spectral variations evident in the map of Anderson et al. (1991); such variations may not be reliable because of missing short u-v spacings. In Figure 2, color represents the spectral index and brightness represents the total intensity at C band, after spatial filtering to remove structures larger than 10″ (see Fig. 3 in AR).

The most striking aspect of Figure 2 is the collection of steep (red) compact features found outside the radio ring. In the west, a group of steep knots is also found projected inside the ring; the velocities are highly turbulent in this region, and we expect that this may be the result of a collision with a dense external cloud (see AR and Keohane & Rudnick 1995). A collection of relatively flat knots is found in the jet region to the northeast. The northern section of the ring is flatter than the rest of the ring.

Figure 3 compares the distribution of spectral indices measured for epochs 1985 and 1987, computed with and without the normalization discussed in § 2.3. The normalization procedure has tightened the correlation between the two epochs, although a small offset from zero-net spectral change remains ($\langle \alpha_{87} - \alpha_{85} \rangle \sim 0.03$) for the set of compact features.

2.6. *A Search for Temporally Varying Spectral Indices*

Given the rapid evolution of the radio-emitting material in Cas A, we might also expect to see temporal variations in the particle energy distribution. We test for secular changes in spectral index by comparing the quantities ($\alpha_{87} - \alpha_{85}$) and ($\alpha_{90} - \alpha_{87}$) for each knot in our sample. Given the problems associated with the 1990 L-band observations, we do not expect a strong correlation between these quantities; however, even a small positive correlation would indicate true spectral variability.

A Spearman rank correlation test has been applied to these two sets of spectral change data, both for the whole sample and for subsamples defined by knot brightness, radius, fractional brightness change, and spectral index. For no grouping did we find any significant correlation between ($\alpha_{87} - \alpha_{85}$) and ($\alpha_{90} - \alpha_{87}$). Restricting the correlation test to only knots which have errors in spectral change less than 0.05 (56 knots total) did not improve the strength or significance of the correlations. Again, this is not surprising, owing to the poor quality of the 1990 1.4 GHz image.

There still remains the possibility of identifying significant variations using the 1985–1987 data alone. The rms measured in the quantity $\alpha_{87} - \alpha_{85}$ is comparable to the expected error (~ 0.05); thus, the spread apparent in Figure 3 predominantly reflects the noise inherent in the measurements. All knots with spectral change $|\alpha_{87} - \alpha_{85}| > 0.20$ and significance $> 3\ \sigma$ (knots 4, 118, 183, and 212) have been examined firsthand to search for possible unifying traits. Each of these knots is quite faint and shows apparent secular steepening. They do not share any other common characteristics, such as position in the remnant, morphology, fractional rate of brightness change, or residual velocity.

In conclusion, we find no evidence for spectral changes in the knot sample as a whole on timescales of order a few years. A few features do exhibit potential change; verification would require a close inspection for possible confusion (e.g., a merging with line-of-sight knots of differing α). As no clear unifying characteristics can be identified for this set of knots, this will not be pursued further at present.

3. CORRELATIONS BETWEEN SPECTRAL INDEX AND OTHER KNOT PROPERTIES

We now examine the relationship between the spectral indices of radio knots in Cas A and their dynamical properties, e.g., the position of the knot within the remnant, knot brightness, rate of brightness change, and expansion timescale (a measure of deceleration). Readers interested only in the conclusions are invited to skip to § 3.3.

3.1. *Trends with Position*

Table 2 reports the strong rank correlation between knot spectral index and (projected) radial position within the remnant. This correlation is strongest among bright knots, with a tendency toward steeper indices beyond the radio ring.

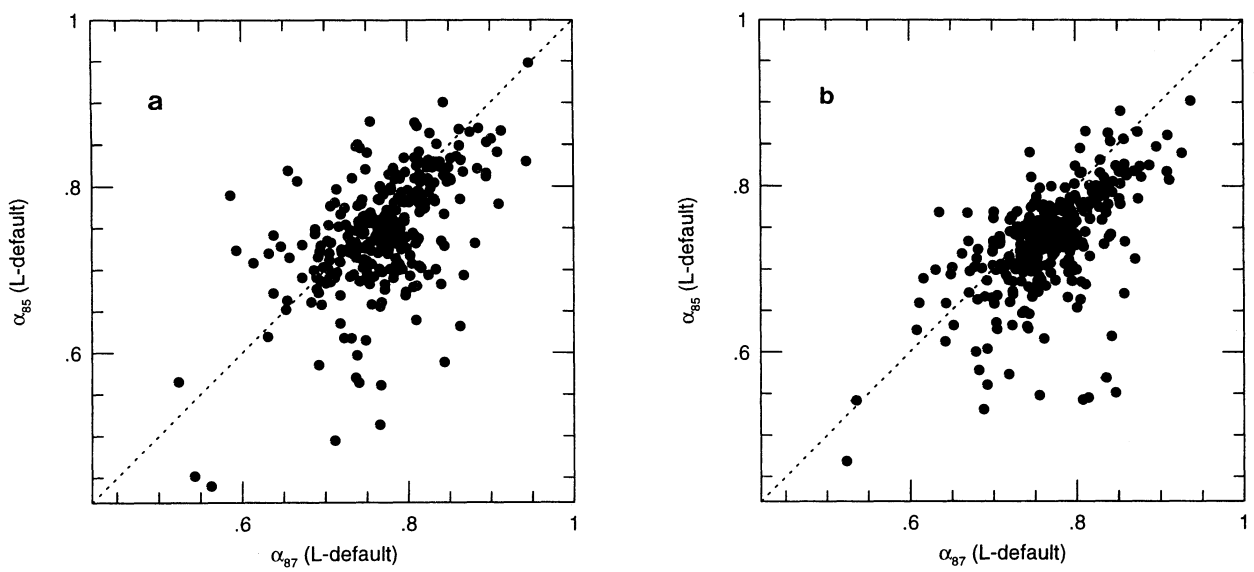

FIG. 3.—A comparison of spectral indices measured for epochs 1985 and 1987, shown (*a*) with and (*b*) without normalization

TABLE 2

RESULTS OF SPEARMAN RANK CORRELATION TEST[a]

SUBSET	NUMBER OF KNOTS	α VERSUS R		α VERSUS B	
		r_s	$P(r_s)$	r_s	$P(r_s)$
All knots	304	0.22	0.00012	0.21	0.00021
Faint knots	152	0.19	0.02	0.05	0.52
Bright knots	152	0.27	0.00092	0.19	0.017
Fading knots	99	0.14	0.17	0.16	0.12
Brightening knots	205	0.23	0.00072	0.23	0.00078
Inner knots	139	0.05	0.53	0.26	0.0022
Outer knots	165	0.24	0.0022	0.20	0.01
Eastern knots	122	0.22	0.013	0.19	0.035
Western knots	181	0.24	0.001	0.18	0.015

[a] For correlations between radio knot spectral index, projected radius (R), and brightness (B); r_s is the rank coefficient of correlation and $P(r_s)$ is the two-tailed probability that the given distribution satisfies the null hypothesis (see, e.g., Press et al. 1992, p. 634). The cutoff between bright/faint knots is 12.2 mJy beam^{-1}, and the cutoff between inner/outer knots is a radius of 100″.

Figure 4 shows histograms with bins in projected radius for the flattest ($\alpha < 0.77$) and steepest ($\alpha > 0.82$) knots in the remnant. It is clear that these two subsets are located in distinctly different volumes within the remnant. The distributions are reasonably well-described by shells of inner and outer radii 95″–130″ (flat) and 140″–170″ (steep; see models overlain on Fig. 4). The radial distribution of flat knots is very similar to that of the bright, diffuse radio ring, which also shows relatively flat spectral indices (Anderson et al. 1991; Fig. 2). The low-resolution observations of Kassim et al. (1985) also suggest that the bright ring is flatter than the outlying regions.

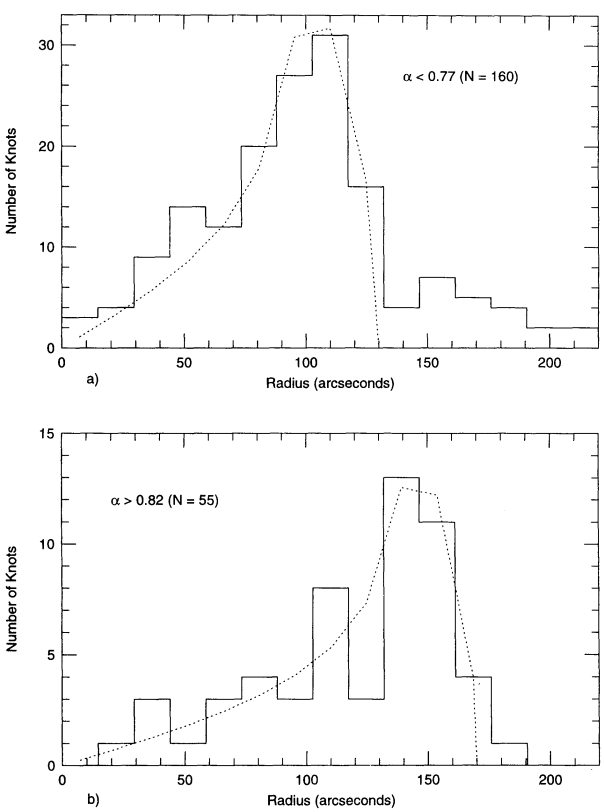

FIG. 4.—Histograms of projected radial position for (*a*) knots flatter than $\alpha = 0.77$ and (*b*) knots steeper than $\alpha = 0.82$. Overlain in dotted lines, for comparison, are models of shells with uniform knot distributions and inner and outer radii (*a*) 95″–130″ and (*b*) 140″–170″.

In addition to the two shell-like distributions, there is a population of faint knots found at large radii that form the tail of the flat spectrum population in Figure 4. These knots are located predominantly in the jet region to the northeast, a region which optical studies have identified as unique on compositional and dynamical bases (see, e.g., van den Bergh & Kamper 1985; Kamper & van den Bergh 1976).

We have verified that these radius/radio spectrum trends are not an artifact of our normalization procedure; they are present at similar levels among the unnormalized spectral indices.

3.2. *Trends with Brightness*

Table 2 also shows that spectral index is correlated with knot brightness, with steeper knots tending to be brighter. A more detailed examination of this correlation can be seen in Figure 5, where plots of α versus knot brightness for epochs 1985 and 1987 are shown. An error-weighted estimate of the offset in mean α between knots brighter and fainter than 25 mJy beam^{-1} yields $|\Delta\langle\alpha\rangle| = 0.027 \pm 0.003$ for both epochs, with fainter knots being spectrally flatter. Such a skewing can be instrumental in origin when spectra are calculated by simple division of interferometric images, as used by Anderson et al. (1991). Here, however, all large-scale offsets between images have been removed in the regression; thus, our spectra are immune to such flux-related biases.

In addition to the mean spectral index being steeper for bright knots, the scatter in α for knots brighter than 25 mJy beam^{-1} is real; their spread is 3 (5) times greater than expected from noise alone for the 1985 (1987) data. Below 25 mJy beam^{-1}, the broadening of the distribution in α is consistent with noise.

While a rank correlation between spectral index and knot brightness exists, this relation should not be interpreted as a *general* tendency for all bright knots to be steeper. The observed correlation is primarily caused by a set of bright, steep knots lying outside the noise envelope in Figure 5. In examining these knots individually, we find that they are

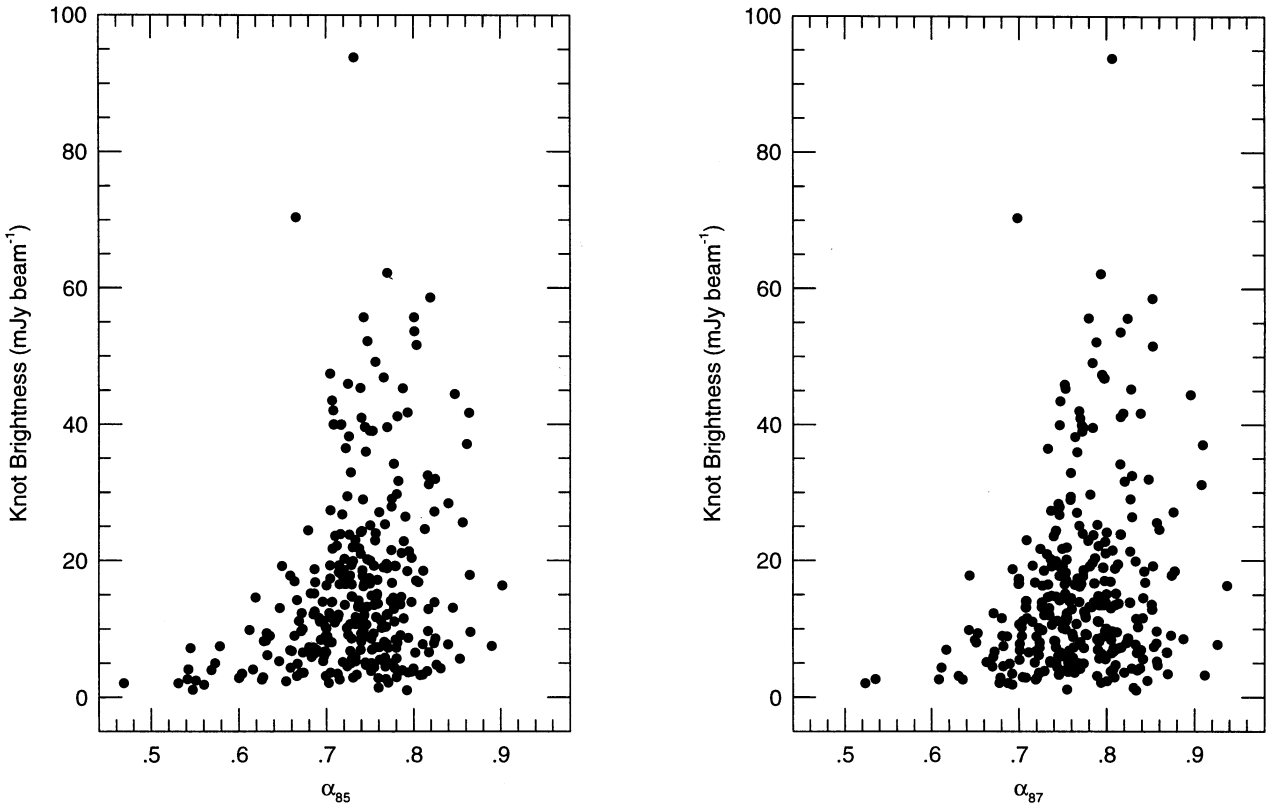

FIG. 5.—Spectral index vs. knot brightness for epochs 1985 and 1987, computed with image normalization

located primarily beyond the radio ring, and in fact they are a subset of the knots that drive the spectral index/radius correlation.

3.3. *Trends with Spectral Index—Summary*

The most significant finding to arise from this comparison is the fact that spectrally steep and flat compact features appear to reside in two different volumes within Cas A. The flattest knots are found in the bright radio shell, while the steepest knots occupy an exterior shell, coincident with the diffuse plateau. How such spectral segregation may pertain to models of particle acceleration within the remnant is pursued further in § 5.

We find also that there is a population of bright, steep knots, found primarily at large radii, that yield a brightness/steepness correlation for the sample.

4. EVIDENCE FOR PARTICLE ACCELERATION IN CAS A

Before we continue our search for sites of particle acceleration in Cas A, we first establish the need for a current acceleration of relativistic particles within the remnant. Given the new dynamical and spectral data, we find that most previously used arguments for current acceleration are no longer valid. The only remaining compelling argument for particle acceleration in Cas A involves the high emissivities observed in many compact features within the remnant. In particular, we will demonstrate that the high emissivities associated with the radio bow shocks require an enhancement in the density of relativistic electrons over that available from simple shock compression of the background cosmic-ray population. These results can be used to place constraints on the relevant injection pool.

4.1. *A Reevaluation of Arguments for Particle Acceleration in Cas A*

4.1.1. *Flux Density Decay Rate*

One argument that has been put forth in the past (e.g., Drury 1983) in support of active particle acceleration in Cas A is the fact that the observed rate of flux density decay is less than that expected from the Shklovsky (1960) Σ-D relation for an adiabatically expanding spherical nebula. If the remnant's diameter, D is growing at a rate $D \propto t^x$ ($x = 1$ implies free expansion), then Shklovsky's relation predicts a fractional rate of brightness change given by

$$\frac{\Delta S_\nu}{S_\nu} \sim -\frac{\beta x}{t}\ \mathrm{yr}^{-1}\ , \tag{5}$$

where $\beta = 2(2\alpha + 1)$, and t is the remnant's age ($\sim$313 yr at the time of writing; Ashworth 1980). In the absence of a consistent measurement of bulk radio expansion, this argument has been based on the assumption that Cas A is expanding on a timescale commensurate with the undecelerated optical knot proper motions ($T \sim 300$ yr; van den Bergh & Kamper 1983). Inserting the integrated spectral index of Cas A ($\alpha = 0.77$) into equation (5), we obtain $\Delta F_\nu/F_\nu \sim -1.7\%\ \mathrm{yr}^{-1}$, which is significantly greater than the observed decay rate of $\sim -0.9\%\ \mathrm{yr}^{-1}$ (Baars et al. 1977). Lequeux (1962) generalized the expression in equation (5) to the geometry of an expanding shell and found only a slight decrement in the expected rate of decrease. The retarded rate of decay in Cas A's synchrotron flux has

often been attributed to an in situ generation of relativistic particles.

This argument was challenged by Green (1988) on the basis of measurements of the bulk expansion of the radio remnant, which gave an expansion timescale between 380 and 460 yr. At a timescale of 460 yr, there is no need for current particle acceleration on these grounds. AR revisited this measurement of bulk expansion and obtained a much stronger challenge to the arguments for acceleration. The minimum expansion age reported by AR (750 yr) predicts, from equation (5), a rate of integrated flux density decrease on the order of $-0.7\%\ \mathrm{yr}^{-1}$; the longest age (1300 yr) yields an estimate of $-0.4\%\ \mathrm{yr}^{-1}$. Both limits predict rates slower than the $\sim -0.9\%\ \mathrm{yr}^{-1}$ observed; thus, ongoing particle acceleration is *not* required by the Shklovsky model. We must seek other evidence to support the claim for particle acceleration. That the observed decline is faster than our revised expections may be a result of the simplified nature of the Shklovsky model. For example, time-decaying magnetic field strength (e.g., through reconnection dissipation) may hasten the fading.

4.1.2. *Secular Spectral Flattening*

The apparent secular flattening of the integrated synchrotron spectrum of Cas A (Baars et al. 1977) led Scott & Chevalier and collaborators (Scott & Chevalier 1975; Chevalier, Robertson, & Scott 1976; Chevalier, Oegerle, & Scott 1978) to pursue an explanation in terms of active particle acceleration. They modeled this flattening with an ongoing second-order Fermi acceleration of particles in turbulent vortices, generated in the wakes of the optical knots as they passed through the diffuse remnant material.

The frequency dependence of decay in the integrated spectrum of Cas A is now being questioned on the basis of new measurements by Hook et al. (1992). We must await the acquisition of further evidence before we can evaluate this argument for ongoing particle acceleration.

4.1.3. *Polarization Arguments*

Turbulent acceleration was also proposed by Dickel & Greisen (1979) as a solution to the observed secular flattening. Their argument was based on the fact that total intensity and polarized intensity in Cas A are spatially anticorrelated at $\lambda = 11$ cm. Such a condition could occur if localized reductions in polarized intensity result from higher levels of turbulence; such regions would also be brighter (as observed) if relativistic particles are locally accelerated. This argument for turbulent acceleration was adopted by Cowsik & Sarkar (1984) in constructing a detailed model for the evolution of synchrotron luminosity in Cas A.

Anderson, Keohane, & Rudnick (1995), however, have demonstrated that there is no evidence for an anticorrelation between polarized and unpolarized intensities at $\lambda = 6$ cm. Instead, they show that an increased local density of thermal particles (along with the relativistic plasma) is responsible for the depolarization observed by Dickel & Greisen (1979). Again, the argument for particle acceleration fails.

4.2. *Arguments for Particle Acceleration Based on Radio Knot Emissivities*

Braun, Gull, & Perley (1987, hereafter BGP) identified a set of paraboloidal structures seen in Cas A as bow shocks driven by dense clumps of ejecta. The synchrotron emissivities of BGP's features A–J, tabulated in Table 3 along with their associated minimum energy and pressure-derived quantities, range between 10^{-20} and 10^{-19} ergs s^{-1} cm^{-3}. These emissivities represent an enormous increase, 10^{10}–10^{11} times, over a typical interstellar value of $\approx 10^{-30}$ ergs s^{-1} cm^{-3} (see, e.g., measurements quoted by Badhwar, Daniel, & Stephens 1977). The minimum energy fields listed in Table 3, on the order of a few milliGauss, are also quite high in comparison with the average Galactic magnetic field, ~ 3 μG. The increase in field strength of $\sim 10^3$ cannot be achieved by simple compression at a strong, nonradiative shock, which yields at most a gain of 4.

There are persuasive arguments for accepting these minimum energy field values as being indicative of the actual conditions in Cas A. As noted by Anderson et al. (1991), the large amount of energy inferred from minimum energy considerations for the radio-emitting plasma (~ 3–4×10^{49} ergs in the ring alone) is already uncomfortably close to Braun's (1987) estimate of 1.5×10^{50} ergs in the kinetic energy of the diffuse ejecta of Cas A. Small departures of the magnetic field from its minimum energy value result in dramatic increases in inferred energy content. Furthermore, Bell (1977) points out that if the

TABLE 3

MINIMUM ENERGY/PRESSURE CALCULATIONS FOR BOW SHOCKS[a]

		Minimum Pressure			Minimum Energy		
Label	ϵ (ergs s^{-1} cm^{-3})	B (mG)	Energy (ergs)	Pressure (ergs cm^{-3})	B (mG)	Energy (ergs)	Pressure (ergs cm^{-3})
A	1.9×10^{-20}	2.1	$6.4 \times 10^{+44}$	4.0×10^{-7}	2.8	$5.6 \times 10^{+44}$	4.6×10^{-7}
B	3.4×10^{-20}	2.8	$8.2 \times 10^{+44}$	7.3×10^{-7}	3.8	$7.2 \times 10^{+44}$	8.5×10^{-7}
C	1.4×10^{-20}	2.1	$8.3 \times 10^{+44}$	4.2×10^{-7}	2.9	$7.3 \times 10^{+44}$	4.9×10^{-7}
D	1.5×10^{-20}	2.2	$8.6 \times 10^{+44}$	4.3×10^{-7}	3.0	$7.6 \times 10^{+44}$	5.0×10^{-7}
E	1.1×10^{-19}	3.6	$1.0 \times 10^{+45}$	1.2×10^{-6}	4.9	$9.1 \times 10^{+44}$	1.4×10^{-6}
F	4.9×10^{-20}	3.0	$1.4 \times 10^{+45}$	8.3×10^{-7}	4.1	$1.3 \times 10^{+45}$	9.6×10^{-7}
G	3.3×10^{-20}	2.6	$6.6 \times 10^{+44}$	6.2×10^{-7}	3.5	$5.8 \times 10^{+44}$	7.2×10^{-7}
H	4.1×10^{-20}	3.0	$1.0 \times 10^{+45}$	8.2×10^{-7}	4.1	$8.9 \times 10^{+44}$	9.5×10^{-7}
I	1.8×10^{-20}	2.2	$1.2 \times 10^{+45}$	4.3×10^{-7}	3.0	$1.1 \times 10^{+45}$	5.0×10^{-7}
J	4.4×10^{-20}	2.6	$7.2 \times 10^{+44}$	6.4×10^{-7}	3.6	$6.3 \times 10^{+44}$	7.4×10^{-7}
Ring.....	9.5×10^{-22}	0.9	$3.7 \times 10^{+49}$	7.4×10^{-8}	1.2	$3.3 \times 10^{+49}$	8.6×10^{-8}

[a] Minimum energy/pressure-derived quantities for bow shocks A–J. Calculations assume a distance of 2.9 kpc and a relativistic proton-to-electron density ratio of 100, typical of the Galactic cosmic-ray population. Total emissivity, ϵ, is computed integrating between observing frequencies of 10^7 and 10^{11} Hz, assuming a constant spectral index over this range as given in Table 1.

fields were significantly less than their minimum energy values, the pressure in the compact radio knots would vastly exceed the confining pressure of the fluid behind the blast wave. Therefore, we adopt these minimum energy values in the following discussion, realizing that this necessitates the invocation of some nonadiabatic field amplification mechanism active *prior* to the formation of the bow shocks.

One such mechanism has been proposed by Gull (1973, 1975). Gull's model predicts that as the ejected material in an SNR begins to decelerate, Rayleigh-Taylor fingers of relatively cold and dense ejecta drip into the hot fluid residing behind the outer blast wave. Secondary Kelvin-Helmholtz instabilities generate turbulence in a thin boundary layer surrounding the fingers, creating new magnetic field energy through turbulent dynamo effects.

However, even after amplifying the field to 3 mG (typical of the bow shocks), Anderson et al. (1991) point out that simply placing the observed cosmic-ray flux of $367E^{-3.15\pm0.2}$ electrons m^{-2} sr^{-1} s^{-1} GeV^{-1} (Golden et al. 1984) in such a field results in a synchrotron emissivity a factor of 10^4 lower than observed. Only small gains in emissivity (1 order of magnitude) can be achieved through adiabatic compression of the CR population at the outer blast wave (compression at the weak bow shocks is negligible in comparison). Therefore, we conclude that relativistic particle acceleration, i.e., nonadiabatic energization processes, must be invoked to match the observed emissivities.

The fact that synchrotron spectral indices in Cas A tend to steepen with increasing feature brightness provides further evidence that particle acceleration, as opposed to simple adiabatic compression, is occurring within the remnant. If the cosmic-ray electron population does steepen at higher energies (e.g., Tang 1984), as is also suggested by the Galactic synchrotron background (see, e.g., discussion in Longair 1981), a simple compression model for spectral variations would predict that regions of higher magnetic field (the bow shocks and bright knots) would appear flatter than regions where the field was lower (the ring), contrary to what is observed. It is interesting to note how this argument is used in extragalactic sources, in which high emissivities and spectral flattening (the opposite of Cas A) are used as evidence for particle acceleration (see, e.g., Meisenheimer et al. 1989).

In the following sections, we will look in more detail at possible sites for relativistic particle acceleration. We will conclude with the apparent paradox that while relativistic particle acceleration must be ongoing in Cas A, it is probably *not* associated with the features that are currently bright in radio emission. One possible model of how this can occur is discussed in AJKTR.

4.3. *Bow Shocks as Possible Particle Acceleration Sites*

If, as was argued on dynamical grounds by BGP and AR, the paraboloidal structures identified by BGP are truly bow shocks, then this emission must arise from a fluid which has recently passed through a shock of Mach number commensurate with the observed proper motion and geometry. We have already seen that their emissivities cannot be explained simply by shock compression of cosmic-ray electrons.

Bell (1978) derives an expression (his eq. [11]) describing the synchrotron emissivity obtainable from first-order shock acceleration of particles from a thermal pool. We can use this expression to estimate the emissivity expected from bow shock C, assuming that the dominant seed population in Cas A is derived from the background thermal pool. Bow shock C exhibits a proper motion of 4300 km s^{-1} (AR). If the blast wave is expanding at a velocity of 1670 km s^{-1} (as is implied, given certain assumptions, by the high-temperature X-ray component in Cas A [Fabian et al. 1980] and by the geometry of the bow shocks [AR]), then bow shock C is traveling at a velocity $\sim(4300 - \frac{3}{4} \times 1670) = 3050$ km s^{-1} relative to the post–blast-wave fluid. We adopt Bell's suggested values of $\psi_e = 4$ for the energy above which thermal electrons are injected into the acceleration cycle (in units of $\frac{1}{2}m_p v_s^2$) and $\phi_e = 0.001$ for the injection efficiency. Assuming a magnetic field strength of 3 mG behind the bow shock, $\alpha = 0.88$ (from Table 1), a thermal density of $n = 2$ cm^{-3} (e.g., Downs & Thompson 1972) and integrating between 10^7 and 10^{11} Hz, an emissivity of 6×10^{-19} ergs s^{-1} cm^{-3} is obtained. The observed emissivities are easily reproduced.

We now consider the observed spectral index of feature C. In the first-order, test particle limit, a Mach M shock in $\gamma = 5/3$ gas will yield an equilibrium spectral index

$$\alpha = \frac{M^2 + 3}{2(M^2 - 1)} . \tag{6}$$

A Mach number of 2.3, as estimated by BGP for bow shock C from the feature's opening angle, is then expected to give $\alpha = 0.97$, quite close to the observed spectral index of 0.88, especially since the observed Mach number is likely to be an underestimate of the true asymptotic opening angle, which is reached far from the region in which radio emission is easily visible.

We could also estimate the emissivity expected if the relevant injection pool is assumed to be the Galactic cosmic-ray electron population: that the injection of thermal electrons into the acceleration mechanism is insignificant. Here we encounter a paradox. All cosmic rays now residing in the post–blast wave medium *must* have been processed by the blast wave itself. Since the blast wave is still strong, the injection pool should therefore (excluding shock-modification effects) have a preinjection energy index of $p = 2.0$, translating to a spectral index of $\alpha = 0.5$. The bow shocks are considerably steeper than this, although there is no known way to *steepen* a population at a shock. The synchrotron lifetimes of these particles are far too long to account for this discrepancy through aging. Therefore, if these features are indeed bow shocks, and if they are truly traveling in the post–blast-wave region (as indicated by their geometry and proper motions; AR), the injection of thermal particles at the bow shocks must strongly dominate the injection of cosmic rays. If, however, a means can be found by which Cas A's blast wave could be so strongly modified by internal cosmic-ray pressure that it generates an equilibrium energy index of >3, injection from the cosmic-ray pool must be reconsidered (see Jones & Kang 1993).

In summary, the acceleration of relativistic particles appears necessary to explain the emissivities observed in compact features in Cas A. We find that first-order acceleration can account for the emission from bow shock features, although these structures may or may not be the major sites of particle acceleration in the remnant. The seed particles for acceleration must be freshly injected from the thermal pool at the bow shocks; they cannot be derived from the Galactic cosmic-ray population, barring a strong modification of the blast wave. The flatter spectral indices in the diffuse ring and knots from this region will require another acceleration scheme.

5. WHAT REGULATES SPECTRAL INDEX—KNOT-INTRINSIC OR ENVIRONMENTAL EFFECTS?

In the preceding section, we showed that particle acceleration must be occurring in Cas A and argued that this is plausible physically, at least in the bow shocks. We now examine the implications of the various correlations discussed in § 3 between spectral index and other properties of the knots. In particular, we compare the observational evidence with two generic types of models for regulating the spectral indices: (a) the spectral variations merely reflect regional variations in the relativistic electron populations in the intraremnant fluid or (b) knots with different spectra are intrinsically different from each other, dynamically or otherwise, leading to differences in particle acceleration. In the discussion to follow, we will refer to these hypotheses, respectively, as "environmental" and "knot-intrinsic" spectral regulation.

We begin by summarizing the observational evidence and show that environmental models are much more consistent with the data; intrinsic knot properties may play a partial, but less significant, role. Then we discuss the properties of possible environmental models in more detail.

5.1. *The Observational Case for Environmental Spectral Regulation*

The key argument in support of an environmental model is that no other physically important variable allows as clean a separation of knots into distinct spectral populations as does radius. This fact is reiterated in Figures 6*a*–6*d*, where the histograms indicate the spectral indices of knots subgrouped by cuts in brightness, fractional change in brightness, inverse expansion timescale, and projected distance from the remnant center. Annuli of radii 80″–120″ and 130″–180″ were chosen for the radial cutoff in Figure 6*d* to isolate the limbs of the steep and flat shells in Figure 4. Results of a Kolmogorov-Smirnov comparison between the distributions shown in Figures 6*a*–6*d* are tabulated in Table 4. Among these, segregation by radius yields the most distinct distributions in α. This statement is relatively independent of the exact choice of cutoff levels. It is remarkable that such a small difference in spectral index as that which defines the two populations ($\Delta\alpha \sim 0.05$) can produce such radically different spatial distributions. Whatever process regulates the observed spectral index must only *slightly* modify the indices between the two regions and do so quite uniformly. This places great constraints on the nature of the hypothesized regulating factor.

Note, however, that the spectral distributions of knots segregated by brightness are also statistically different, as is evidenced in Figure 6*a* and Table 4. The fainter knots have a distribution in spectral index consistent with Gaussian noise, but the bright knot distribution is distinctly non-Gaussian and is skewed toward steeper indices. The knots which are bright and steep do form a distinct group. This argues for some intrinsic connection between the underlying physical processes;

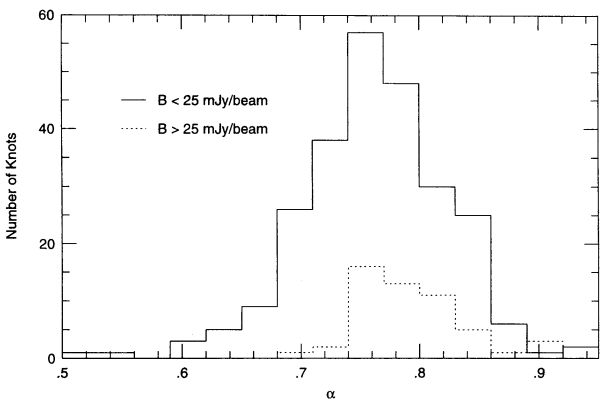

FIG. 6*a*

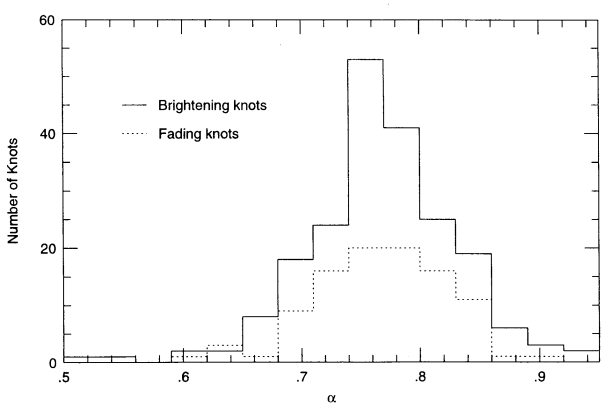

FIG. 6*b*

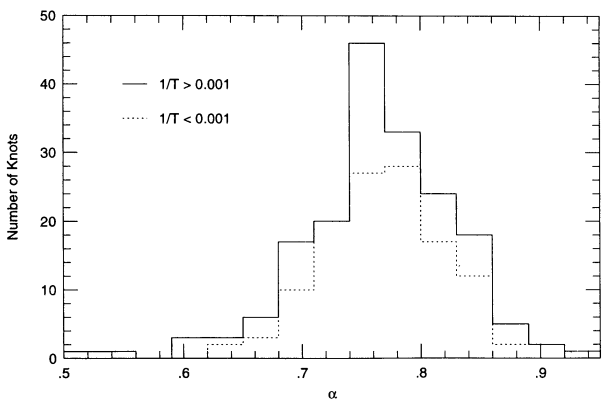

FIG. 6*c*

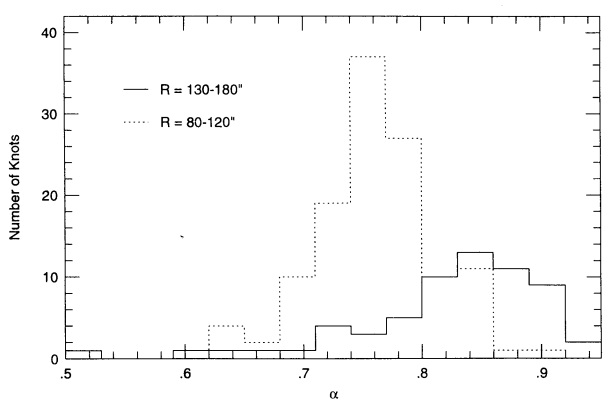

FIG. 6*d*

FIG. 6.—Histograms of spectral index for knot subsamples segregated by (*a*) knot brightness, (*b*) annual fractional brightness change, (*c*) inverse expansion timescale (yr^{-1}), and (*d*) projected radius from the remnant expansion center.

TABLE 4

RESULT OF K-S TEST[a]

Cutoff Type	N_{low}	N_{high}	D	Probability (D)
B	252	52	0.311	0.02
dB/B	99	205	0.068	0.29
$1/T$	124	180	0.079	0.25
R	122	65	0.419	0.003

[a] Results of a Kolmogorov-Smirnov comparison between distributions displayed in Fig. 6. Rows apply, in order, to segregation by brightness, fractional brightness change, inverse expansion timescale, and radial annuli. N_{low} gives the number of knots lying below the specified cutoff, and N_{high} gives the number above the cutoff. D is the K-S static derived for each distribution pair, and the probability of obtaining a statistic greater than D under the null hypothesis is given in the last column.

however, this correlation is much weaker than the positional dependence and is probably secondary. Most of the bright steep knots are found *outside* the radio ring in the plateau region. Furthermore, there are instances of bright flat knots; these are found almost without exception in the vicinity of the ring (BGP's feature J, for example).

The fact that the spectral indices of compact features in the ring do not differ significantly from that of the broad-scale ring emission offers further evidence for an environment-based spectral regulation. In spectral index maps generated from a ratio of L- and C-band images (Anderson et al. 1991), radio knots in the ring are typically indistinguishable from their immediate surroundings. Also, the recent results of Kassim et al. (1995) suggest that the total emission beyond the ring may be following the same steepening trend as we see in the compact features.

X-ray observations (e.g., Fabian et al. 1980) of Cas A provide additional evidence that the environmental conditions in the ring and plateau differ strongly. These observations suggest two concentric shells of differing temperature: an inner, cooler shell, coincident with the radio ring, and an outer, hotter shell, presumably the blast wave–heated interstellar medium (ISM). The X-ray temperatures measured by Fabian et al. (1980) for regions outside the X-ray ring (their outer two annuli) and in the ring (the third and fourth annuli) are shown as histograms in Figure 7. While a detailed spatial correlation between modeled temperature and average spectral index could not be found, each parameter leads to the same pair of concentric

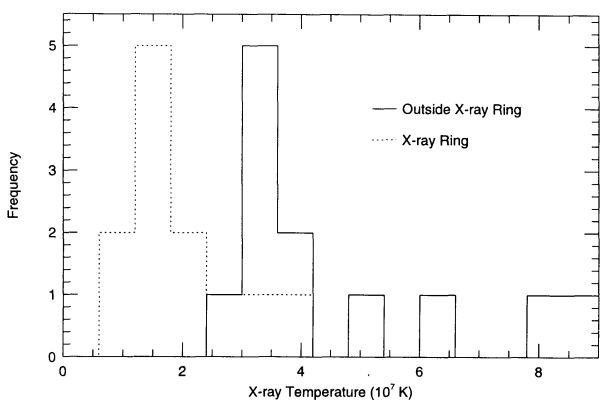

FIG. 7.—Histogram of X-ray temperatures derived for regions outside and in the X-ray ring (data from Fabian et al. 1980).

shells. Azimuthal variations in temperature in the X-ray plateau also fit this pattern; the temperature derived for the base of the jet is cooler than temperatures found in other regions of the X-ray plateau, and it is here that an anomalously flat congregation of synchrotron spectral indices is found (see Fig. 1). New spatial temperature maps anticipated from *ROSAT* or *ASCA* observations would allow a more detailed test of these general correspondences.

We now consider some of the consequences of knot-intrinsic spectral regulation models. We might assume, e.g., that physical conditions in the knots near the ring are different because they are interacting with a much denser, probably turbulent medium. Such physical differences could easily lead to spectral differences; however, it is hard to see why some other physical parameters are not affected even more strongly, such as expansion timescale or rate of brightness change. While a relationship with knot brightness is found, the separation into unique spectral populations on this basis is not clean.

Another possibility is that the shocks formed by knots in the ring are stronger (hence flatter) than those associated with the outer knots. Since bright knots are more heavily decelerated, their leading bow shocks might then be weaker, yielding steeper spectra. However, the correlation between spectral index and knot deceleration is relatively weak. In addition, we do find bright knots near the ring which are very flat; in these cases, some other factor has superseded the shock strength effect, and it is this factor which is most important to identify.

5.2. *Environment-based Spectral Regulation Scenarios*

One way to decouple the observed physical properties of a knot from its spectrum is if the relativistic particles were accelerated at some earlier time and now merely find themselves radiating in the enhanced magnetic field within the feature. The spectral index of the feature then reflects the spectral index of the local background population of relativistic particles. This background must be produced by some form of stellar ejecta; as discussed in § 4, it is unlikely that they have been processed by the outer blast wave. For example, the background could be produced by previous generations of bow shocks driven by undecelerated (unseen) ejecta clumps. Indeed, the simulations of Jones et al. (1994) predict that a moving clump's productive lifetime (in terms of accelerating particles) is almost over by the time the clump becomes visible as a radio source.

This type of scenario relaxes the need for strong correlations between spectral index and knot brightness, brightness change, and deceleration; all the particles have been accelerated (i.e., the spectral index is determined) before the knot in question becomes visible. Secondary correlations may still exist as a result of environmental effects on magnetic field amplification, etc., although these properties themselves do not directly control the observed spectral indices.

We must still explain the variations in the background particle spectral indices, but we must do it in a way not directly coupled to the currently visible knots. One possible explanation is that different acceleration mechanisms are at work within different regions in the remnant, each generating a characteristic population of relativistic particles. For example, particles outside the ring may be generated primarily at bow shocks, while particles near the ring may undergo some reacceleration in enhanced turbulence localized near the contact discontinuity. Figure 6*d* shows that a viable reacceleration mechanism active in the ring must only slightly alter the spectral index of the background population.

Another possibility is that the spectral index at a given radius is a function of the average bow shock strength of clumps that have penetrated to or beyond that radius. As clumps decelerate with distance from the explosion center, the associated bow shocks progressively weaken, and they leave behind steeper and steeper populations of accelerated particles. The jet region may have formed through the ejection of clumps with preferentially high velocities; thus, bow shocks in this region would be expected to be stronger on average, yielding a flatter background population of relativistic particles.

Alternatively, the background temperatures may dominate the shock strength variations, with lower Mach numbers occurring in high-temperature regions. This explanation fits with the temperature distribution inferred from X-ray observations as described in § 5.1. The degree of spectral variation that can be expected from the observed temperature variations can be estimated to first order. A typical Mach number of $M_{\rm ring} = 2.9$ is required to produce the observed spectral index of $\alpha = 0.77$ at the ring. Assuming similar clump velocities in both regions, a Mach number given by

$$M_{\rm out} \sim M_{\rm ring}\sqrt{\frac{T_{\rm ring}}{T_{\rm out}}} \quad (7)$$

should be typical in regions outside the ring. Using the modes of temperature distributions plotted in Figure 7, we find $M_{\rm out} = 2.0$, implying that spectral indices of $\alpha_{\rm out} = 1.2$ should be typical in this region. The predicted difference is somewhat larger than the observed spectral variations.

6. CONCLUSIONS

We conclude that particle acceleration has indeed occurred in Cas A; the high synchrotron emissivities observed in the radio knots of Cas A cannot be explained by simple adiabatic shock compression of cosmic rays from the Galactic background. This remains true even if we allow for a strong, nonadiabatic growth in magnetic field strength within the knots, as is implied by the observed minimum energy fields. Some type of particle energization, or reenergization, process is required to generate the abundance of relativistic electrons inferred for these features. Given the relatively steep spectral indices associated with these features ($\alpha > \sim 0.8$), it appears that most of the particles injected into the relevant acceleration mechanism have been derived from the pool of thermal particles residing within the remnant. The pool of Galactic cosmic rays which have entered the remnant through the blast wave would be too flat ($\alpha \sim 0.5$) to account for such steep spectral indices.

The absence of significant correlations between the dynamical and spectral properties of radio knots in Cas A, in conjunction with a strong dependence on position (within or outside of the bright radio ring), is most consistent with a scenario in which the knots reflect the slope of the relativistic electron distribution in the medium through which they move. In our interpretation, the knots themselves have not accelerated the particles which currently illuminate them; these particles have merely diffused into the knots from the background intraremnant plasma and now radiate in the amplified field therein. This is a somewhat novel interpretation, as it implies that *bright synchrotron features are not dominant sites of current particle acceleration* within the remnant. Most of the acceleration occurs while a clump of ejecta is radio quiet or driving a faint bow shock. This would imply that features are not bright because they are currently accelerating a large abundance of fresh relativistic particles, but rather because interactions with the surrounding medium have triggered strong magnetic field amplification. The background populations themselves may radiate weakly in magnetic fields introduced to the post–blast-wave region by Rayleigh-Taylor fingers emanating from the contact discontinuity, thus forming the plateau emission.

This lesson must be remembered when interpreting spectral variations in other shell remnants in which emission features are perhaps not so well understood as in Cas A. It must not be assumed a priori that observed spectral variations are necessarily tied to well-defined synchrotron features (see also G41.1 − 0.3; Anderson & Rudnick 1993).

We gratefully acknowledge the work of R. Perley, R. Braun, and S. Gull in obtaining some of the Cas A data, and N. Kassim and especially T. W. Jones for many helpful comments. We thank the only responding referee, K. Meisenheimer, for his prompt review. The work presented here was supported at the University of Minnesota in part by the NSF through grants AST 91-00486 and AST 93-18959, and by the Minnesota Supercomputer Institute.

REFERENCES

Anderson, M. C. 1993, Ph.D. thesis, Univ. Minnesota
Anderson, M. C., Jones, T. W., Rudnick, L., Tregillis, I. L., & Kang, H. 1994, ApJ, 421, L31 (AJRTK)
Anderson, M. C., Keohane, J. W., & Rudnick, L 1995, ApJ, 441, 300
Anderson, M. C., & Rudnick, L. 1993, ApJ, 408, 514
———. 1995, ApJ, 441, 307 (AR)
Anderson, M. C., Rudnick, L., Leppik, P., Perley, R., & Braun, R. 1991, ApJ, 373, 146
Ashworth, W. 1980, J. Hist. Astron., 11, 1
Avni, Y. 1976, ApJ, 210, 642
Baars, J. W. M., Genzel, R., Pauliny-Toth, I. I. K., & Witzel, A. 1977, A&A, 61, 99
Badhwar, G. D., Daniel, R. R., & Stephens, S. A. 1977, Nature, 365, 424
Bell, A. R. 1977, MNRAS, 179, 573
———. 1978, MNRAS, 182, 443
Braun, R. 1987, A&A, 171, 233
Braun, R., Gull, S. F., & Perley, R. A. 1987, Nature, 327, 395 (BGP)
Chevalier, R. A., Oegerle, W. R., & Scott, J. S. 1978, ApJ, 222, 527
Chevalier, R. A., Robertson, J. W., & Scott, J. S. 1976, ApJ, 207, 450
Cowsik, R., & Sarkar, S. 1984, MNRAS, 207, 745
Dickel, J. R., & Greisen, E. W. 1979, A&A, 44
Downs, G. S., & Thompson, A. R. 1972, AJ, 77, 120
Drury, L. O'C. 1983, Rep. Prog. Phys., 46, 973
Fabian, A. C., Willingale, R., Pye, J. P., Murray, S. S., & Fabbiano, G. 1980, MNRAS, 193, 175
Golden, R. L., Mauger, B. G., Badhwar, G. D., Daniel, R. R., Lacy, J. L., Stephens, S. A., & Zipse, J. E. 1984, ApJ, 287, 622
Green, D. A. 1988, in Supernova Remnants and the Interstellar Medium, ed. R. S. Roger & T. L. Landecker (Cambridge: Cambridge Univ. Press), 205
Gull, S. F. 1973, MNRAS, 161, 47
———. 1975, MNRAS, 171, 263
Hook, I. M., Duffett-Smith, P. J., & Shakeshaft, J. R. 1992, A&A, 255, 285
Jones, T. W., & Kang, H. 1993, ApJ, 402, 560
Jones, T. W., Kang, H., & Tregillis, I. 1994, ApJ, 432, 194
Kamper, K., & van den Bergh S. 1976, ApJS, 32, 351
Kassim, N. E., Perley, R. A., Dwarakanath, K. S., & Erickson, W. C. 1995, ApJ, submitted
Keohane, J., & Rudnick, L. 1995, ApJ, submitted
Lequeux, J. 1962, Ann. d'Astrophys., 25, 221
Longair, M. S., 1981, High Energy Astrophysics (Cambridge: Cambridge Univ. Press)
Meisenheimer, K., Röser, H.-J., Hiltner, P. R., Yates, M. G., Longair, M. S., Chini, R., & Perley, R. A. 1989, A&A, 219, 63
Napier, P. J., Thompson, A. R., & Ekers, R. D. 1983, Proc. IEEE, 71, 1295
Press, W. H., Teukolsky, S. A., Vetterling, W. T., & Flannery, B. P., 1992, Numerical Recipes in Fortran (Cambridge: Cambridge Univ. Press)
Scheuer, P. A. G., 1984, Adv. Space Res., 4, 2–3, 337
Scott, J. S., & Chevalier, R. A. 1975, ApJ, 197, L5
Shklovsky, I. S. 1960, Soviet Astron., 4, 355
Tang, K.-K. 1984, ApJ, 278, 881
Tuffs, R. J. 1986, MNRAS, 219, 13
van den Bergh, S., & Kamper, K. W. 1983, ApJ, 268, 129
———. 1985, ApJ, 293, 537